HII Regions + PN + AGN

Strömgren sphere : uniform density, fully ionized sphere

$$\mathcal{N}_{recomb} = \mathcal{N}_{ioniz}$$

$$\frac{4\pi}{3} R_S^3 \, n_e n_p \beta_B = \mathcal{N}_{Lyc}$$

B: case B neglects recomb to n=1

$$R_S \approx 1\,pc \left(\frac{10^3}{n}\right)^{2/3} \left(\frac{\mathcal{N}_{Lyc}}{3\times10^{49}}\right)^{1/3}$$

(O5 ★)

neutral fraction $\sim 10^{-3}$ ⟹ little opacity (?)

½ of Lyc photons must be absorbed in 1/2 of volume

— 0.8 R_S

How does M_{HII} depend on n?

$$M = \frac{4\pi}{3} R_S^3 \, n_p m_p = \mathcal{N}_{Lyc} \frac{m_p}{n_e \beta_B}$$

$$\simeq 100\, M_\odot \frac{\mathcal{N}_{Lyc}}{3\times10^{49}} \frac{10^3}{n_e}$$

H + He are almost fully ionized until ionization front where all ionizing photons are used up.

Other elements don't use up ionizing photons

Their ionization state is determined by ioniz-recomb. balance which varies w/ R as F_{Lyc} falls as R^{-2}.

Important parameter : $U = \frac{n_{Lyc}}{n_e} = \frac{F_{Lyc}}{n_e c}$

ionization parameter

Heating + Cooling in HII Regions

Dust: heating by absorbing stellar radiation
heating by absorbing Lyα
cooling by emission of IR
$\Rightarrow T_d \sim 300$ K (silicate emission)

Gas: heating by ionization
$A + \gamma \rightarrow A^+ + e^- + (KE = h\nu - IP \sim kT_*)$
$A^+ + e^- + KE \rightarrow A + \gamma$ $KE \lesssim \frac{3}{2} kT_e$
photoelectric ejection of e^-'s from grains
Y ~ few % (so probably not so important)
cooling by ff emission
important in pure H nebula, but not very effective
$\Rightarrow T_e \sim T_* - 10^4$ K
cooling by collisionally excited line radiation
negligible for H unless T ~ 50,000 K (?)
most important: visible forbidden lines + IR fine-structure
of NII, OIII (0.5, 52, 88 μm), OIV (25 μm), OII (0.37)
SIV (10.5 μm), SIII (0.9, 18, 33 μm)
visible lines are good thermostats $\Rightarrow T_e \sim 10^4$ K
note: for $n_e < n_{cr}$, heating + cooling $\propto n^2$
if $n_e > n_c$, cooling $\propto n^1$

S. Hwang + H. Dinerstein: abundances from ORLs > CELs in PNe
optical CELs only probe hot gas
cold, metal-rich gas only probed by RLs
pressure equilibrium?

ISM Phases

50 yr ago : HI + HII

by 40 yr ago : H_2, WNM + CNM

later : WIM, HIM

HI Carbon ionization : IP = 11.3 eV

ionized except in molec. clouds

(all other metals too except N, O, F, Ne)

[CII] (158 μm) seen in mol clouds - holey?

Heating : UV ionization of atoms, PAHs, dust

CR, XR important at $n \lesssim 1$ shocks?

Cooling : [CII] + [OI] 63 μm in CNM (diffuse HI clouds)

Lyα in WNM - why not [OI] (6300 Å) ?

cooling at const n : $n^2\Lambda \propto T^{-1/2} + e^{-E_{Ly\alpha}/kT}$

for $n_e < n_{cr}(CII)$, $T_e > E_{CII}$

but n isn't const. instead $n = P/kT$

so $n^2\Lambda \propto (T^{-1/2} + e^{-E_{Ly\alpha}/kT})\,T^{-2}$

heating : $n\Gamma_{pe} \propto \varepsilon n G_0$ (FGH assume cr heating)

$\varepsilon \sim .05$ for $\gamma \leq 300$ $\gamma = G_0 T^{1/2}/n_e$

$\propto 1/\gamma$ for $\gamma \geq 300$

$n\Gamma \propto n G_0$ for $n_e > .03$ $T = 100$ $G_0 = 1$

$\propto n^2 T^{-1/2}$ $n_e < .3$ $T = 10^4$ $G_0 = 1$

at const. P :

$\Rightarrow n\Gamma \propto T^{-1}$

$\rightarrow$ or $T^{-2.5}$

So if [CII] dominates cooling there is no good thermostat. If T increases, cooling falls more than heating does. Until Lyα cooling turns on.

Can trapped Lyα cause cooling?

Why is Lyα cooling important (instead of [OI]) in WNM, but small (vs. [OIII]) in HII regions?

1) $n_H(\text{WNM}) > n_H(\text{HII})$ b/c $1-x \sim 10^{-3}$

$n_{O^{++}}(\text{HII}) > n_O(\text{WNM})$ b/c $n_{HII} > n_{WNM}$

2) $\gamma(O^{++}-e^-) > \gamma(O-H)$

WIM Seen by WHAM

Must be ionized by EUV from OB *s.

How does it penetrate so far?

HIM next page

skip 8.7, 8.8 Vertical Distribution

Eqn. of Hydrostatic Equil: $\frac{dP}{dz} = -g\rho$

Assume $g, T =$ const, $P = nkT$

$$kT \frac{dn}{dz} = -gmn$$

$$\Rightarrow n = n_0 e^{-z/H} \qquad H = \frac{kT}{gm} \quad \text{(atmosphere)}$$

In galaxy or accretion disk: $g = \dot{g} z$

$$\frac{dn}{dz} = -\frac{\dot{g} m}{kT} z n$$

$$\Rightarrow n = n_0 e^{-z^2/2H^2} \qquad H^2 = \frac{kT}{\dot{g} m}$$

$\dot{g} = 2.2 \times 10^{-11}$ cm s^{-2} pc^{-1} $\qquad g \sim \frac{4\pi}{\wedge} G \rho_{*s} z^3/z^2$

$H(\text{CNM}) \sim 20$ pc $\qquad \dot{g} \sim \frac{4\pi}{\wedge} G \rho_{*s}$

$H(\text{WNM}) \sim 200$ pc

$\approx$ Oort limit $\rightarrow \rho_{*s} \sim 10^{-23}$ g/cm^3 $\sim .1\ M_\odot/\text{pc}^3$

HIM — Shock heating by SNR expansion creates another phase

$kT \sim m_H v_{SN}^2 \sim 10^6$ K

SNRs overlap + form network of bubbles + tunnels which may fill ~1/2 of ISM, esp. in halo.

No continuous heating, but cooling time is long because density is low.

Chemistry — simple molecules, radicals in CNM

H_3^+ drives much of chemistry

formation: $H_2 + CR \rightarrow H^+ + H + e^-$

$H^+ + H_2 \rightarrow H_3^+$

destruction: $H_3^+ + CO \rightarrow HCO^+ + H_2$ (in MC)

$H_3^+ + e^- \rightarrow H_2 + H$ (in HI)

equilibrium: $n_{H_3^+} \propto J_{CR}\, n_{H_2}/n_{CO}$ or $J_{CR}\, n_{H_2}/n_{e^-}$

note: not $\propto$ density

± same in CNM, MCs

21 cm — H $(I+S = F = 1-0)$ $\Delta E/k = .07$ K

$$\tau_{21cm} = 5.5\times10^{-21}\, N_H \left(\frac{1\ \mathrm{km\,s^{-1}}}{\sqrt{\pi}\, b}\right)\left(\frac{100K}{T}\right)$$

$\simeq 0$ in WNM ← why?

$$T_b = \tau T = 5.5\times10^{-19}\, N_H \left(\frac{1\ \mathrm{km\,s^{-1}}}{\sqrt{\pi}\, b}\right)$$ indep of T

Pulsar dispersion

$$v_{gr} = \left\{1 - \frac{\nu_p^2}{\nu^2}\right\}^{1/2} c \qquad \text{for } \nu \gg \nu_p = \left(\frac{n_e e^2}{\pi m_e}\right)^{1/2}$$

- longer λs travel more slowly ~ 1 kHz

$$\delta t = \frac{e^2}{2\pi m_e c \nu^2} \underbrace{\int n_e \, dl}_{D}$$

D: dispersion measure

Faraday rotation

$$v_{ph} = c\left\{1 - \frac{\nu_p^2}{\nu(\nu \pm \nu_B)}\right\}^{-1/2} \qquad \pm = \frac{RCP}{LCP}$$

$$\nu_B = eB_\parallel / 2\pi m_e c$$

- causes rotation of linearly polarized waves

$$\Delta\theta = \frac{\pi}{c\nu^2} \int \nu_p^2 \nu_B \, dl \qquad (\text{from } R+L = \text{Tielens} / 2\pi)$$

Molecular Hydrogen

molecular orbitals λ, parity

$1\sigma_g^2 \Rightarrow {}^1\Sigma_g \rightarrow 1s\ 1s$

$1\sigma_g 1\sigma_u \Rightarrow {}^3\Sigma_u \rightarrow 1s\ 1s$

$1\sigma_g 1\pi_u \Rightarrow {}^1\Pi_u, {}^3\Pi_u \rightarrow 1s\ 2p$

in ${}^1\Sigma_g$ electronic state:

$E_{vJ} = hc\omega_e(v+\frac{1}{2}) + hcB_e J(J+1) - \cdots$ $\quad \bar{\nu} \approx \omega_e \Delta v + B_e 2J\Delta J$

$\omega_e = 4160\ cm^{-1}$ (2.4 μm)

$B_e = 60\ cm^{-1}$

proton spatial exchange symmetry = parity = $(-1)^J$

$\Rightarrow I = 0$ requires J = even para $g=1$

$I = 1$ J = odd ortho $g=3$

$\Delta J = \pm 2, 0$ (quadrupole xitions w/ $A \propto \nu^5$)

O, Q, S

rotational levels are thermalized $\quad n_{cr}(2-0) = 10$, $3-1$ 300

vibrational levels usually aren't

excitation: thermal at high n, T

fluorescent at low n, high UV

$n_{cr}(H-H_2) \sim 10^5\ cm^{-3}$

$n_{cr}(H_2-H_2) \sim 10^{10}\ cm^{-3}$

dissociation: on ~10% of UV absorptions

gas heating: fluorescent excitation + coll deex.

C_2H_2 ortho/para like H_2

quadrupole rot xitions at $\lesssim$ 1 mm not observed

vibration breaks sym. $\Rightarrow$ P, Q, R dipole xitions

must have ortho + para for each J in $v=1$

CO

ASTRONOMY 393F 11/20/09

Dan Jaffe

Getting Properties of Molecular Clouds From Observations

I. Total Cloud Column Density

Method 1: Submillimeter dust emission

$$S_\nu = B_\nu(T)\,\Omega\,(1-e^{-\tau_\nu})$$

R. Hildebrand (1983), QJRAS 24, 267

1. Measure Flux at some submm λ. [Device?
2. Estimate the temperature [? How
3. Use these to derive τ_ν
4. N_{H+H_2} = const x τ_ν, where do we get const?
   a. Q_{UV}/Q_{IR} from PDR
   b. Q_{UV}/N_{H+H_2} from UV extinction + H_2

? Advantages / disadvantages

Method 2: Dust Extinction

NICER - Lombardi & Alves 2001 A&A 377, 1023

$\sigma(H-K)^{tr} \simeq 0.08$ - mean colors of stars in the IR have very little scatter.

Standard reddening curves give you $A_V/(H-K)$

$$A_V = 15.87 \cdot \left[(H-K)^{obs} - (H-K)^{tr}\right]$$

1. Use background stars (2MASS or own images)
2. Spatially average colors.
3. A_V/N_{H_2} from UV H_2 + H

? Advantages / disadvantages

Method 3: Column density of molecule / Abundance

We measure a T_B and ΔV

$$I_\nu \Delta\nu = \frac{2kT_B}{c^2}\nu^2 \, \nu \frac{\Delta V}{c} = 2kT_B \Delta V \frac{\nu^3}{c^3}$$

$$I_\nu \Delta_\nu = \frac{h\nu}{4\pi} A_J N_u$$

$$A_J \propto |\mu|^2 \quad \text{- dipole moment}$$

total colum density

$$N = \frac{N_J}{2J+1} e^{-[hB\,J(J+1)/kT]} \quad U$$

U is the partition function $\cong \frac{kT}{hB}$ for $hB \ll kT$ and LTE.

This is, for example $C^{18}O$. How do we get to N_{H_2}?

a) Through extinction. -

b) UV CO/H_2

c) 1-0 S(0) and CO absorption lines

$\Rightarrow$ 10% of C in CO $\;{}^{16}O/{}^{18}O \sim 500$.

Advantages / Disadvantages ?

\- Freezeout, PDR, τ not $\ll 1$

\+ Easy, ~~works in most clouds~~,
doesn't necessarily miss small lumps

II. Cloud Mass

Method 1: Sum up column densities
(see previous problem)

Method 2: Virial Mass
$E = \frac{1}{2}\langle U \rangle$
$\Rightarrow \quad \Delta v = \left(\frac{GM}{R}\right)^{1/2}$

measure cloud size + width of lines
advantages / disadvantages ?

Method 3: CO Magic number
$N_{H_2}/I_{CO} = \text{const} \simeq 3\times10^{20}\ \text{cm}^{-2}\ (\text{K km s}^{-1})^{-1}$

Maloney & Black (1988)
How calibrated? – vs. Method I + 2
γ-rays
Physical meaning – virialisation + temperature

Advantages / disadvantages

IV Dust temperature

Measure S_ν vs ν

but note that (a) $Q_\nu \neq$ const

and T is almost never a constant.

Typically, the measured T is a function of the ν @ which you measure.

Why is this?

V. Gas temperature

Method 1: Measure an optically thick line.

T_{MB} is what you measure. $= (1-e^{-\tau})T_{ex}$

Is this $\equiv T_K$ Why not?

(a) Beam error pattern

(b) Source doesn't fill beam

(c) Rayleigh-Jeans approximation not valid

— example of CI line in cold clouds

(d) $T_{ex} \neq T_K$

Method 2: Symmetric Tops (CH_3CN) or NH_3 Inversion Lines

Trick is to find something with metastable states (NH_3) or with different energies @ Exc − why?

Use Boltzmann eqn. Non-LTE effects

Problems: Chemistry + excitation

Opacity

Diatomic — measure different frequency transitions

→ Rotation diagram

VI Density

Method 1: Column density / size

Method 2: Mass / volume

Method 3: N_J vs J — non-LTE means populations drop first in upper states if T is held constant but n decreases.

Puzzle: Method 3 almost always gives much bigger numbers than methods 1 & 2. How can this be?

(a) Observational selection effect — what is it?

(b) Physical effect — what is that?

VII Cloud Kinematics

(A) Turbulence —

a) Doppler Broadening FWHM $= \sqrt{\frac{8kT\ln 2}{m}}$ in velocity units

measure 2 species w/ different m.

b) $V(x,y)$

(B) Infall — optically thick line signature

(C) Outflow — bipolars

(D) Shocks

(6)

VIII Electron Abundance
Wootten et al. 1979

11/23

10.36 $$I_{ul} = \frac{N_u A_{ul} h\nu_{ul}}{4\pi}$$

10.38 $$T_B \Delta v = 10^{-5} \left(\frac{c^3}{2k \nu_{ul}^3} \right) I_{ul}$$

10.40 $$N_u = g_u \left(\frac{kT_x}{hcB} \right) N_{CO} \exp(-E_u/kT)$$ [sic]

rotation diagram

$\frac{4\pi I_{ul}}{A_{ul} h\nu_{ul}} \frac{1}{g_u}$ vs E_u

opt depth curve of growth

mix of T's

non-LTE n_{cr} vs. J

$A_{ul} \propto \nu^3 \propto J_u^3$

fig 9.14 T_{rot}, T_{vib}

avoiding non-LTE w/ metastable states

C_2H_2 vs HCN

NH_3

$$N_{H_2} = \frac{N_{^{18}CO}}{X_{18} X_{CO}}$$

Tielens: $X_{18} X_{CO} = 1.7 \times 10^{-7}$ from reddening

$\Rightarrow X_{CO} = 8.5 \times 10^{-5} \Rightarrow$ 10% of C in CO

Lacy: $X_{CO} \sim 2 \times 10^{-4}$

how to measure T_{gas}, N_{gas}, n_{gas}

how to measure T_{dust}, N_{dust}, a_{dust}

were ignored, the two functions $E_g(R)$ and $E_u(R)$ would coincide, the resulting curve being repulsive at all distances.

The electron probability density in the states Φ_g and Φ_u is given by $|\Phi_g|^2$ and $|\Phi_u|^2$, respectively, so that the corresponding charge densities are $\rho_g = -e|\Phi_g|^2$ and $\rho_u = -e|\Phi_u|^2$ (or $\rho_g = -|\Phi_g|^2$ and $\rho_u = -|\Phi_u|^2$ in atomic units). If the charge density ρ_g is evaluated at points between A and B along the internuclear line, it is found to be greater (in absolute value) than the sum of the densities due to two isolated H atoms with their protons placed at A and B, normalised so that half an electron is associated with each proton. It is this *excess of negative charge* between the protons which causes the binding (or bonding). On the other hand, if the charge density ρ_u corresponding to the antibonding case is evaluated, a *deficiency of negative charge* is found between the protons. This is clearly seen in Fig. 9.10 where the wave functions Φ_g and Φ_u as well as the absolute value of the charge densities ρ_g and ρ_u are plotted along the internuclear line.

The *exact* binding energy of H_2^+ is a little greater than the result obtained above, with $D_e = E_{1s} - E_g(R_0) = 0.103$ a.u. $= 2.79$ eV, and the true equilibrium distance is $R_0 = 1.06$ Å. The principal failing of the approximate wave function $\Phi_g(\mathbf{R}; \mathbf{r})$ given by [9.47a] is that at small separations Φ_g should approach the wave function of $He^+(1s)$, the ground state of the positive helium ion with nuclear charge $Z = 2$, and in the approximation [9.47a] it does not. This defect can be remedied by using orbitals of variable charge, such as

$$u_{1s}(Z^\star, r) = \left(\frac{Z^{\star 3}}{\pi}\right)^{1/2} e^{-Z^\star r} \qquad [9.58]$$

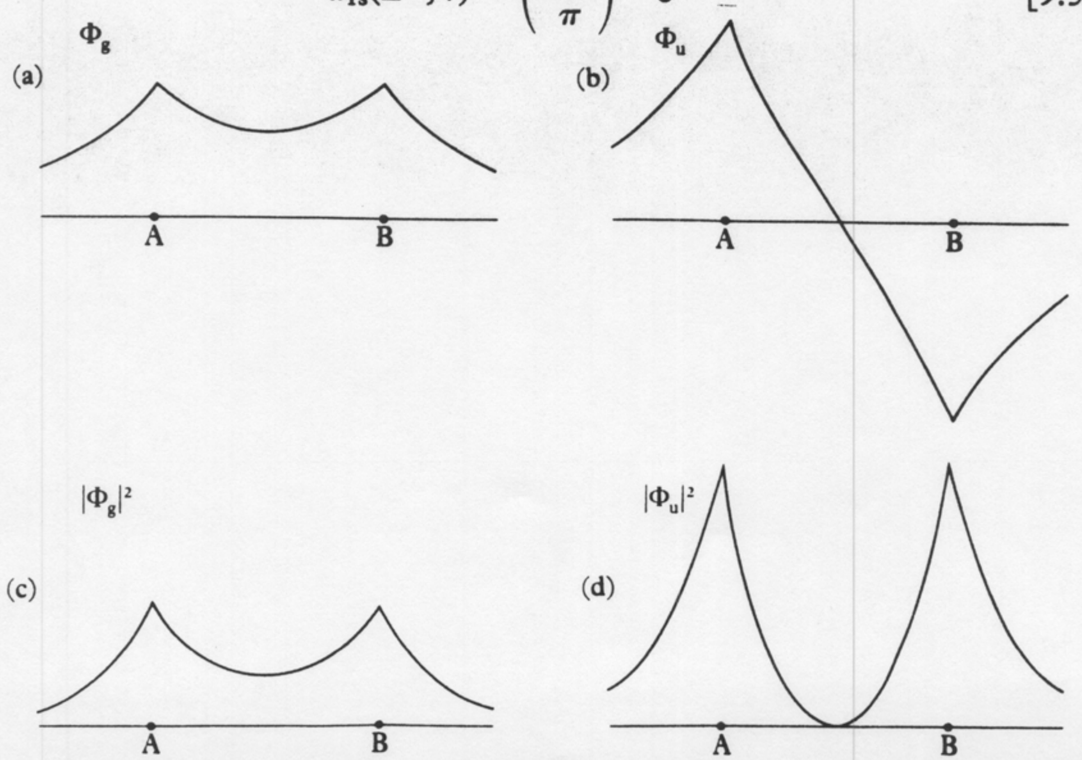

9.10 Wave functions Φ_g and Φ_u and charge densities $|\Phi_g|^2$, $|\Phi_u|^2$ for the hydrogen molecular ion H_2^+, plotted along the internuclear line to an arbitrary scale. The points A and B represent the electronic state, R and J are identical. Rotational levels are normally denoted by N and are assumed to be split into three components if S is 1.

The energy of each state is written (Herzberg 1950, Huber & Herzberg 1979) as an expansion in the quantum numbers (called a term value):

$$T(v,N) = T_e + \omega_e(v + \tfrac{1}{2}) - \omega_e x_e(v + \tfrac{1}{2})^2 + \omega_e y_e(v + \tfrac{1}{2})^3 + \dots$$
$$+ B_v N(N + 1) - D_v N^2(N + 1)^2 + H_v N^3(N + 1)^3 + \dots .$$

T_e is the electronic energy corresponding to the minima in the potential curves. B_v, D_v, etc., are further expanded as power series in $(v + \tfrac{1}{2})$. The constants of the expansion are determined empirically from spectra of the molecule and are usually given in cm^{-1} (Fink et al. 1965, Beck et al. 1979). Use of the formula for very large v or N can lead to errors; some authors prefer to calculate $T(v,N)$

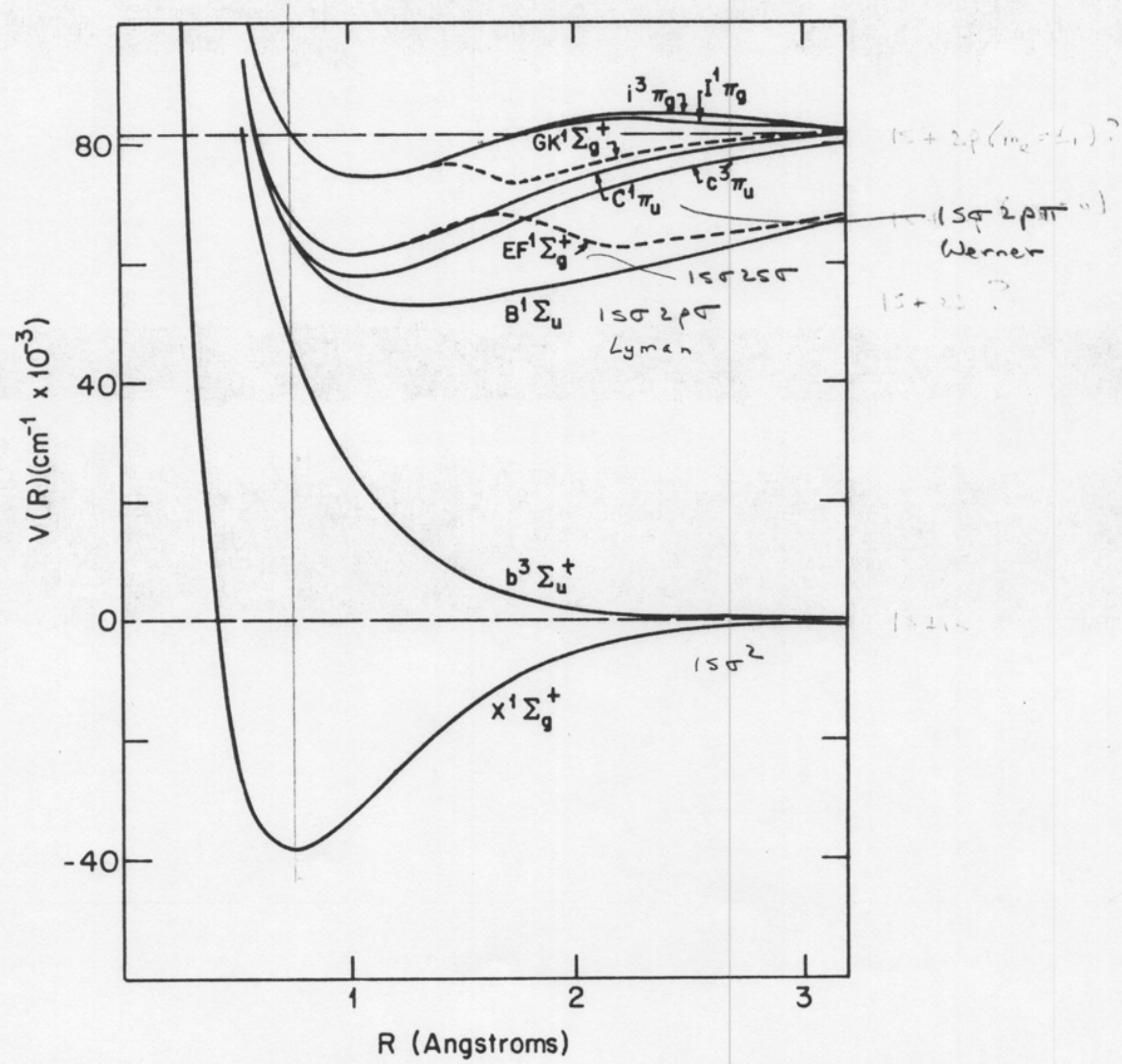

Figure 1 Total energy as a function of internuclear separation for low-lying states of H_2. Horizontal dashed lines denote total energy of two H atoms at infinite separation (both atoms in ground state; one atom in ground state and the other in the first excited states).

Ch 10 esp. 10.7

Molecular Clouds

$He \xrightarrow{CR} He^+ + e^-$

ionization $H_2 \xrightarrow{CR} H_2^+ + e^-$ $\quad\quad C \xrightarrow{UV} C^+$

$e^- \xrightarrow{PAH} PAH^-$

$H_2^+ \xrightarrow{H_2} H_3^+ \rightarrow etc$

recombination $mol^+ + PAH^- \rightarrow mol + PAH$

heating: CR
turb, grav., ambipolar diffusion

cooling: molec. emission (rotational lines)

11/18

---

chemistry: ion-molecule starting w/ H_3^+, C^+
difficulties: E barriers
stability of CO, N_2
leads to simple radicals, C chains,
few saturated molecs.

D chemistry: concentrated in molecs other than HD
b/c $\frac{1}{2}h\nu$ lower + self shielding of H_2
– why is this bigger effect in DCN than in HD?

grain surfaces: how do they overcome E barriers?
favor saturation

condensation/sublimation equil.: (cf vapor pressure)
condens $\propto n_g \sigma_d v_g \propto P$ (approx)
evap $\propto \sqrt{\frac{k}{m}}\, e^{-E_b/kT}$
$\Rightarrow P_{equil} \propto e^{-E_b/kT}$

hot cores: grain mantle evap } more saturated molecs
warm gas chemistry
my obs

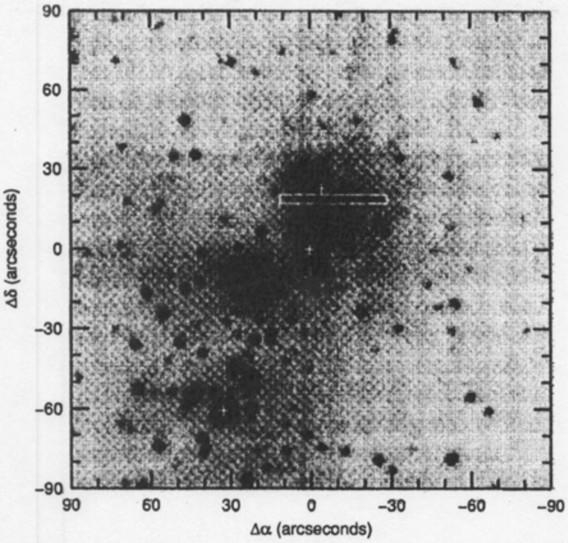

FIG. 2. An image of the brightest H_2 emission and continuum in the central parts of the region shown in Fig. 1. The image is centered on the BN object with north at the top and east to the left. The position of our slit is shown by the box. The three stars marked with plus signs are, from north to south, IRS2, the BN object, and θ^1C Orionis.

Gaussian profiles to the blend components, except in cases of lines too closely spaced in wavelength. Errors in the relative line intensities are primarily due to uncertainties in the estimated continuum level and the flux calibration of the standard star spectrum. The former affects the weakest emission lines, while flux calibration errors affect all of the lines. For the flux calibration to the standard star spectrum we assume an error of $\pm 5\%$ in the relative strengths of all lines, while the continuum uncertainty is estimated independently for each line. The total error adopted for the individual line intensities is computed from the quadrature sum of these two sources of error. The line intensities relative to H_2 $1-0S(1)$

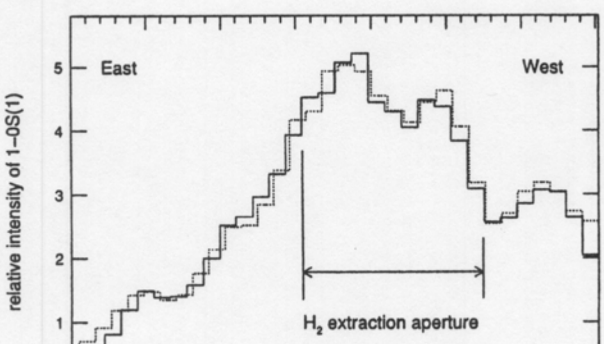

FIG. 3. A plot of the intensity of the $1-0S(1)$ line along our slit is shown as a solid line. The dotted line shows the same region extracted from our continuum-subtracted H_2 image of Fig. 1, using an aperture at the slit position as shown in Fig. 2. The intensity scale has been normalized by an arbitrary constant for both plots so that the intensities match near their peak values. The limits of our 12$''$.1 spectrum aperture is shown.

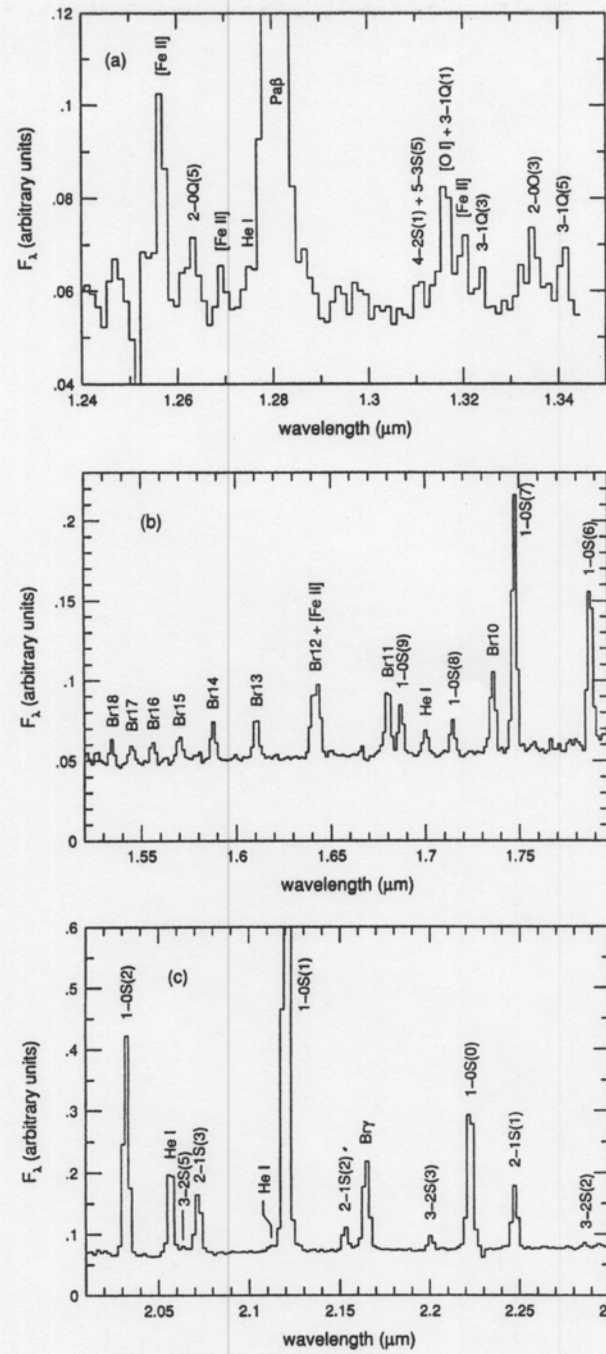

FIG. 4. Spectra of Peak 1 extracted from the slit spectrum as described in the text. The relative intensity has been normalized so that the $1-0S(1)$ line in (c) has a peak intensity above the continuum of 1.

are listed in Table 1 along with their uncertainties and dereddened values (see Sec. 3).

3. EXTINCTION

Our spectra cover a long wavelength baseline with an accurate relative flux calibration. This allows accurate extinction estimates to be made using appropriate line ratios.

fluorescence models, H_2 is formed primarily on grain surfaces and destroyed by the process of spontaneous radiative dissociation as described above. The abundance of H_2 is assumed to be in steady state. The calculation solves the equation of transfer for 22,445 absorption lines simultaneously in a plane-parallel cloud illuminated on one side by an external ultraviolet radiation source. This type of simple geometry is not intended to reproduce the actual distribution of material in AFGL 618. It should, however, produce results which are good averages of the conditions actually present. Also, such models can aid in line identification and verify the presence of fluorescent emission in addition to providing an estimate of the level of excitation by UV photons. Statistical equilibrium equations are solved for the populations of 211 vibration-rotation levels in the $X\ ^1\Sigma_g^+$ state, 629 levels in the $B\ ^1\Sigma_u^+$ state, and 476 levels in the $C\ ^1\Pi_u$ state. Multiple steps are taken through the cloud at each of which the cascade of 2937 vibration-rotation transitions in the $X\ ^1\Sigma_g^+$ state is calculated.

The intensity of the radiation field at the molecular boundary is parameterized by the factor $I_{\rm UV}$, such that $\phi = 4.5 \times 10^{-8} I_{\rm UV}$ photons cm^{-2} s^{-1} Hz^{-1} at $\lambda = 1000$ Å. In regions where the Lyα flux is large, enhanced H_2 excitation might occur due to accidental resonances with the $B\ ^1\Sigma_u^+ - X\ ^1\Sigma_g^+$ $v = 1$–2 $P(5)$ and $R(6)$ transitions, provided that $v = 2$ level in the $X\ ^1\Sigma_g^+$ ground electronic state is already significantly populated. To explore this possibility in AFGL 618, we have examined the effect of a large Lyα flux on the IR fluorescence spectrum.

Thronson (1981) determined an H_2 vibration-rotation excitation temperature based on line fluxes in the 2 μm region that were not corrected for extinction. To minimize error in the thermal model of H_2 emission, we have corrected the fluxes presented by Thronson for $A_V = 3.0$ mag and a standard extinction law. We have determined a new excitation temperature based on the corrected fluxes, even though the change was expected to be small. Assuming a Boltzmann distribution and including all 15 available lines in a least-squares fit to a plot of N_u/g_u versus $T_u = E_u/k$ (see, e.g., Thronson 1981), we found that $T_{\rm ex} = 2250$ K. However, as was also shown by Thronson, the four $v = 2 \rightarrow 1$ lines all appear to be systematically stronger than would be expected for thermal equilibrium, based on the $v = 1 \rightarrow 0$ lines. Since these are also the weakest lines in the spectrum, this might be a result of measurement error. In addition, scatter in the N_u/g_u versus T_u diagram is much larger in the $v = 2 \rightarrow 1$ lines. It therefore seems prudent to leave these lines out of the fit (as was also done by Thronson) and determine a $T_{\rm ex}$ based only on the $v = 1 \rightarrow 0$ lines. For such a least-squares fit, it was found that $T_{\rm ex} = 1942 \pm 200$ K. This can be compared to the value found by Thronson of $T_{\rm ex} = 1950 \pm 200$ K. The difference between the two estimates is completely negligible.

Results of the modeling are presented in Figure 4. A thermal model appears on the bottom, and a fluorescent model is displayed directly below the data. Both models extend into the 2 μm region, and have been adjusted to give the same intensity in the $v = 1 \rightarrow 0$ $S(1)$ line as that given by Thronson (1981). This results in an H_2 column density of $N_{H_2} = 5.2 \times 10^{18}$ cm^{-2} for $T_K = 2000$ K. Characteristics of the spectrum are unchanged if $T_K = 1942$ K. The fluorescent model has been calculated for $I_{\rm UV} = 200$, $n_{\rm H} = 10^5$, and $T_K = 2000$ K. This value of $I_{\rm UV}$ is for a UV radiation field appropriate to a B0 (SC81) star embedded in an H II region, extinguished by about $A_V \sim 1.5$–2.0 mag, and diluted over a distance of $r \approx 10^{17}$ cm,

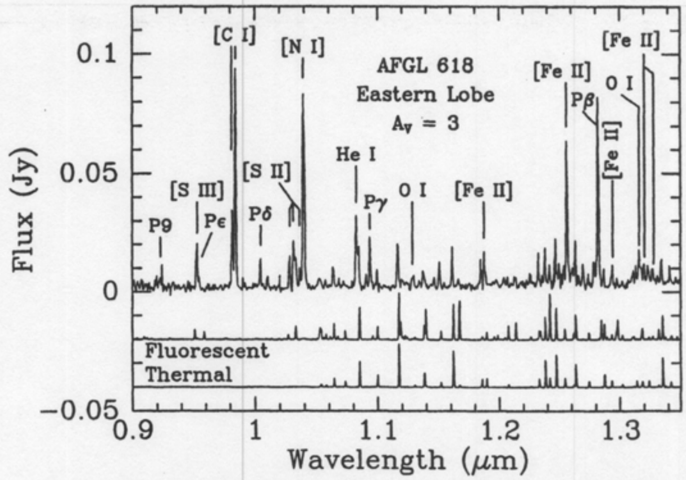

FIG. 4.—Spectrum plotted in Fig. 1 compared with spectral models of thermal and fluorescent emission from H_2. The data appear on top, the fluorescence model in the middle, and the thermal model on the bottom. Parameters for the models are $T_{\rm ex} = 2000$ K and $N_{H_2} = 5.2 \times 10^{18}$ cm^{-2} (thermal), $I_{\rm UV} = 200$, $n_{\rm H} = 10^5$, and $T = 2000$ K (fluorescence; see text). The predicted fluxes have been corrected for $A_V = 3.0$ mag. The flux scale is referenced to the data.

which is comparable to the linear scale of the near-IR lobes in AFGL 618. Both models include $A_V = 3.0$ mag along the observer's line of sight. (We are thus assuming that the extinction to the lobes derived in § 4.1 is entirely interstellar.) It is important to note that these sources of attenuation are separate from the attenuation internal to the lobe, which is calculated using a total gas column density to visual extinction of $N_{\rm tot}/A_V = 6.36 \times 10^{20}$ cm^{-2} mag^{-1}. This is consistent with the gas-to-dust ratio for carbon stars as found by Jura (1986).

A satisfactory fit to the strongest emission lines is produced by the thermal model alone, but the strengths of the weaker molecular hydrogen lines require a fluorescent component. At least four features appear stronger in the data than predicted by either model. These lines include $v = 3 \rightarrow 1$ $S(5)$ (1.152 μm), $3 \rightarrow 1$ $S(3)$ (1.185 μm), $3 \rightarrow 1$ $S(1)$ (1.233 μm), and $2 \rightarrow 0$ $Q(3)$ (1.247 μm). The last two are in a region crowded by other lines. Several models were calculated in which the value of $I_{\rm UV}$ was varied over many orders of magnitude. A better fit than that presented was not obtained. It is possible that these lines are confused with unidentified atomic and/or molecular features. Also, the plane-parallel geometry used in the models might be an inadequate representation of AFGL 618.

In addition, it is important to note that at least three lines are predicted to be stronger by the fluorescence model than observed in the data. These are the $v = 3 \rightarrow 1$ $S(6)$ (1.139 μm), $3 \rightarrow 1$ $S(4)$ (1.167 μm), and $4 \rightarrow 2$ $S(4)$ (1.242 μm) lines. Comparison with a model calculated for a large Lyα flux suggests that these lines can be enhanced by Lyα pumping. Therefore, it would appear that the Lyα flux used in the model shown is too large. The value chosen was based on a simple estimate of the leakage of Lyα photons from the H II region and could easily be an overestimate for a region where dust competes effectively with resonant scattering. A full range in Lyα flux was not explored, however.

While the model fit might not be exact, it is important to note that everywhere a feature is predicted, one is seen. In some cases the detection is marginal, but *no anticoincidences* are found. If we assume that the discrepancies between the model results and the data are due to the complicated geometry

THE ASTROPHYSICAL JOURNAL, 428:L69–L72, 1994 June 20

DETECTION OF ABSORPTION BY H_2 IN MOLECULAR CLOUDS: A DIRECT MEASUREMENT OF THE H_2:CO RATIO

J. H. LACY,[1,2] R. KNACKE,[2,3] T. R. GEBALLE[2,4] AND A. T. TOKUNAGA[2,5]
Received 1994 February 11; accepted 1994 March 31

ABSTRACT

Vibrational absorption by H_2 and CO has been searched for toward infrared sources embedded in molecular clouds. H_2 was detected toward NGC 2024 IRS 2 and possibly toward NGC 2264 (GL 989). CO was detected toward both sources. The results are consistent with the H_2 ortho:para ratio being equilibrated at the cloud temperature. Toward NGC 2024, $H_2:CO = 3700^{+3100}_{-2600}$ (2 σ limits), and toward NGC 2264, $H_2:CO < 6000$. Approximately one-third of all carbon is in gas-phase CO.

Subject headings: infrared ISM: lines and bands — ISM: abundances — ISM: molecules

1. INTRODUCTION

Molecular hydrogen is undoubtedly the most abundant molecule in the interstellar medium. Nevertheless, its abundance has been directly measured only in diffuse clouds, which can be probed by ultraviolet absorption lines. The reason for this is well known; the absence of dipole rotational or vibrational transitions, coupled with the weakness of the quadrupole transitions, makes the opacities of H_2 lines very small, even through dense molecular clouds. In addition, the small moment of inertia of H_2 results in widely spaced rotational levels, which can be excited to emit only under unusual conditions. Because of the difficulty of observing H_2, CO has generally been used as a stand-in, and molecular abundances are typically quoted relative to CO or an assumed H_2 abundance $\sim 10^4$ times that of CO.

Although the bulk of the H_2 in molecular clouds cannot be observed in emission, it is possible to observe it in absorption against bright embedded infrared sources. Both rotational and vibrational absorption lines of H_2 may be detectable, with the vibrational lines being more favorable, due to their greater strengths. CO can also be observed in absorption, through its $v = 0$–1 and $v = 0$–2 vibrational bands. The $v = 0$–2 band is preferred for comparison with H_2 for two reasons: its wavelength proximity to the low-J H_2 lines avoids problems with observations at different wavelengths probing different depths into infrared sources, and its relatively small bandstrength alleviates uncertainties in a curve-of-growth analysis. Black & Willner (1984) and Black et al. (1990) attempted to observe H_2 $v = 0$–1 and CO $v = 0$–2 absorption toward NGC 2024 and NGC 2264. They detected CO and set limits on H_2, requiring $H_2:CO < 1.2 \times 10^4$ toward NGC 2024.

We have repeated the observations of Black & Willner and Black et al., and detected H_2 absorption toward NGC 2024 and possibly toward NGC 2264. We use these observations to make a direct determination of H_2:CO toward these sources.

[1] Department of Astronomy, University of Texas, Austin, TX 78712.

[2] Visiting Astronomer at the Infrared Telescope Facility, which is operated by the University of Hawaii under contract with the National Aeronautics and Space Administration.

[3] Division of Science, Pennsylvania State University, Erie, PA 16563.

[4] Joint Astronomy Centre, Hilo, HI 96720.

[5] Institute for Astronomy, University of Hawaii, Honolulu, HI 96822.

2. OBSERVATIONS

Most of the observations presented here were made with CSHELL, the facility echelle spectrograph at the IRTF (Tokunaga et al. 1990), with W33 observed with CGS4 at UKIRT. CSHELL was used with its 256 × 256 HgCdTe detector array, a dispersion of $\Delta\lambda/\lambda \approx 1.2 \times 10^{-5}$ pixel^{-1}, and a slit image scale on the detector of 0".28 pixel^{-1}. The slit width was 0".5, giving a spectral resolving power of $\sim$40,000. Observations were made at the wavelengths of two H_2 lines, $S(0)$ (4497.84 cm^{-1}) and $S(1)$ (4712.91 cm^{-1}), and 15 CO lines $R(0)$–$R(8)$ (4263–4292 cm^{-1}) and $P(1)$–$P(6)$ (4235–4257 cm^{-1}).

Observations were attempted of seven sources: NGC 2024 IRS 2, NGC 2264 (GL 989), Elias 16, Mon R2, W33A, S140 (GL 2884), and VI Cygni No. 12. Of these sources, only NGC 2024 and NGC 2264 provided useful results for this project; Elias 16 showed a complicated photospheric spectrum, preventing any study of interstellar absorption, VI Cygni No. 12 showed no interstellar lines, and Mon R2, W33A, and S140 showed H_2 emission.

Comparison stars were chosen to be free of interfering spectral features, while being as close as possible to the embedded sources and at least as bright. There are no high spectral resolution surveys of stars in the K band, but visible wavelength spectra show atomic and molecular lines to be present in stars later than A0. Earlier type stars show only hydrogen and helium lines. High ($n' > 20$) Pfund-series lines fall in the region of the CO 0–2 band but are very broad and are not apparent in any of the comparison star spectra. We chose ζ Ori (B0 I, $K \approx 2$) for a comparison star for NGC 2024, and ζ Ori and γ Gem (A1, IV, $K \approx 2$) for comparison stars for NGC 2264. 15 Mon (O7 V, $K \approx 5$) and η Tau (B7 III, $K \approx 3$) also were observed. Comparison of these stars showed two absorption lines in the A1 star γ Gem near the H_2 $S(1)$ line, but not at the frequency of $S(1)$ in NGC 2264. Otherwise, no features were seen in the comparison star spectra.

The observations were made on the nights of 1993 January 24–26, all of which were clear, and October 31–November 2, most of which were cloudy or foggy. Of the results presented here, only the CO P-branch spectra and a confirming $S(0)$ spectrum were obtained on the latter run. Approximately 1 hr of on-source observation time was spent on each of the H_2 settings on each of the embedded sources. About half as much time was spent on each of the CO settings and on the comparison stars.

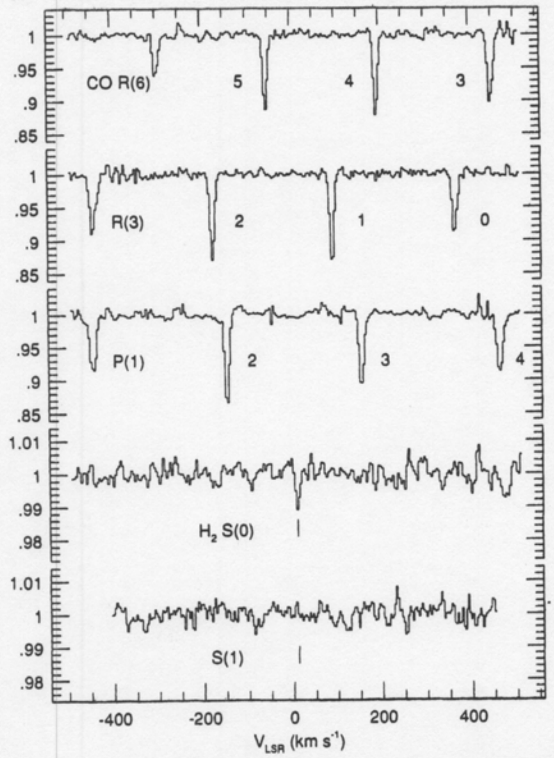

FIG. 1.—Fully processed (including fringe removal) spectra of CO $R(6, 5, 4, 3)$, $R(3, 2, 1, 0)$, $P(1, 2, 3, 4)$, and H_2 $S(0)$ and $S(1)$ toward NGC 2024 IRS 2. The horizontal scale is v_{LSR} for the H_2 lines and is arbitrary for the CO lines. The expected Doppler shift ($v_{LSR} = 10$ km s^{-1}) is marked on the H_2 spectra. Note the differing vertical scales and offsets.

The data were reduced with Snoopy (Achtermann 1992), a program written for reduction of infrared spectroscopic data. Standard procedures were used for flat-fielding, optimal weighting, and division by comparison stars. In addition, the final spectra were divided by a slowly varying function to remove interference fringes. Spectra of NGC 2024 are shown in Figure 1.

3. INTERPRETATION

Since all lines were unresolved, the information in the spectra is contained in the equivalent widths. In the case of CO, the presence of unresolved interfering telluric lines required a correction to the measured equivalent widths in addition to the division by comparison stars. To determine this correction, we modeled the telluric transmission, using the program Atmo (Grossman 1989), adjusting the water vapor until the model, convolved with the CSHELL resolution function, matched our observations of comparison stars. We then multiplied the measured equivalent widths by the ratio of calculated transmission at the wavelength of the observed CO lines to the convolved transmission. This procedure should correct for the actual telluric transmission in the case of very narrow interstellar lines, as we conclude the lines in NGC 2024 and NGC 2264 are.

If a line is optically thin, the column density in the lower state of the transition may be calculated straightforwardly from the equivalent width:

$$N_J(\text{cm}^{-2}) = w_\nu(\text{cm}^{-1})/S_{v,J\to v',J'} ,$$

where S is the line strength factor. For CO,

$$S_{v,J\to v',J'} = \frac{8\pi^3}{3hc}\,\nu\,\frac{\max(J, J')}{2J+1}\,|\mu_{v\to v'}|^2(\text{cm}^{-1}/\text{cm}^{-2}) ,$$

where ν is in cm^{-1}, and $\mu_{0\to 2} = 6.66 \times 10^{-21}$ esu cm (with a weak dependence on J; Goorvitch & Chackerian 1994). For H_2, $S_{S(0)} = 8.2 \times 10^{-26}$ cm^{-1}/cm^{-2}, and $S_{S(1)} = 4.8 \times 10^{-26}$ cm^{-1}/cm^{-2} (Turner, Kirby-Docken, & Dalgarno 1977). For optically thick lines, a saturation correction, or curve-of-growth analysis, is required. We assumed the lines to be Gaussian, and used numerical integration to determine the curve of growth.

The $S(0)$ line of H_2 was detected in absorption toward NGC 2024 IRS 2 with an equivalent width of $(2.4 \pm 0.5) \times 10^{-3}$ cm^{-1}. It was observed on three nights, with consistent results, including the expected Doppler shift change between January and November. The line was centered at $v_{LSR} = 9.5 \pm 2$ km s^{-1}, in agreement with the CO lines. A possible $S(0)$ absorption of $(0.7 \pm 0.6) \times 10^{-3}$ cm^{-1} was seen toward NGC 2264 (GL 989). The $S(1)$ line was not detected toward either source. The H_2 lines must be optically thin; the $S(0)$ equivalent width toward NGC 2024 corresponds to 0.16 km s^{-1}, whereas the H_2 thermal linewidth at the temperature of the CO is 1.0 km s^{-1} (FWHM), requiring a line-center optical depth $\lesssim 0.16$. Derived column densities are given in Table 1.

The measured CO equivalent widths are given in columns (2) and (3) of Table 2. The quoted errors are based on the noise between the lines and our estimates of the uncertainties in the correction for atmospheric absorption, with lines measured on only one night or during poor weather (in November) given higher errors. Column densities, derived assuming the lines to be optically thin, are given in columns (4) and (5), and in Figure 2.

In the case of NGC 2024, the column densities derived from the P- and R-branch lines disagree systematically, in the sense expected if the lines are saturated. We fitted the observations with equivalent widths calculated for a thermal distribution of rotational-state populations and a Gaussian-line curve of growth. A mixture of gas at two temperatures was tried but did not improve the fit. The best-fitting linewidth (e^{-1} half-width), column density, and temperature, and the allowed 2 σ ranges (over which $\chi^2 < \chi^2_{min} + 4$) are $b = 6.9(5.1–8.6) \times 10^{-3}$ cm^{-1}, $N_{CO} = 9.1(6.1–30) \times 10^{18}$ cm^{-2}, and $T = 45(35–54)$ K. The best-fitting distribution of column densities is given in column (6) of Table 2.

The data for NGC 2264 were fitted in the same way as for NGC 2024. In this case the P : R equivalent width ratios do not require saturation, but again the best fit to the shape of the $w_\nu(J)$ distribution was obtained with a single temperature, with

TABLE 1

H_2 EQUIVALENT WIDTHS AND COLUMN DENSITIES

	NGC 2024		NGC 2264	
J	w_ν(cm^{-1})	N(10^{22} cm^{-2})	w_ν(cm^{-1})	N(10^{22} cm^{-2})
0	0.0024(5)[a]	2.9(6)	0.0007(6)	0.9(7)
1	0.0000(5)	0.0(10)	0.0000(8)	0.0(17)
Total[b]		3.5(7)		1.1(8)

[a] 1 σ uncertainties in the last digits are given in parentheses.

[b] Total H_2 column densities assuming a thermal population distribution at the CO temperature.

TABLE 2

CO EQUIVALENT WIDTHS AND COLUMN DENSITIES

J (1)	w_v[a] (cm^{-1}) P (2)	R (3)	N_J(thin)[b] (10^{18} cm^{-2}) P (4)	R (5)	N_J(fit)[c] (10^{18} cm^{-2}) (6)
NGC 2024					
0.....	...	0.015(2)	...	0.19	0.55
1.....	0.018(2)	0.021(1)	0.69	0.39	1.45
2.....	0.022(2)	0.024(2)	0.71	0.49	1.90
3.....	0.018(2)	0.020(1)	0.55	0.42	1.86
4.....	0.018(4)	0.020(2)	0.54	0.43	1.47
5.....	0.017(4)	0.018(1)	0.50	0.39	0.99
6.....	0.009(2)	0.014(2)	0.27	0.30	0.56
7.....	...	0.011(2)	...	0.24	0.28
8.....	...	0.005(2)	...	0.11	0.12
Sum			3.38		9.07
NGC 2264					
0.....	...	0.025(1)	...	0.31	0.43
1.....	0.019(3)	0.043(2)	0.73	0.80	1.07
2.....	0.020(3)	0.036(2)	0.65	0.73	1.24
3.....	0.024(3)	0.029(1)	0.74	0.61	1.00
4.....	...	0.023(1)	...	0.50	0.62
5.....	...	0.015(1)	...	0.33	0.31
6.....	...	0.003(1)	...	0.07	0.12
Sum			3.50		4.70

[a] Measured equivalent widths, with 1 σ uncertainties in the last digits, based on the estimated uncertainty in the correction for telluric absorption, given in parentheses.

[b] Column densities derived assuming the lines to be optically thin. Sum includes only observed states.

[c] Column densities for the best-fitting thermal population distribution, assuming a Gaussian-line curve-of-growth. Sum includes all rotational states.

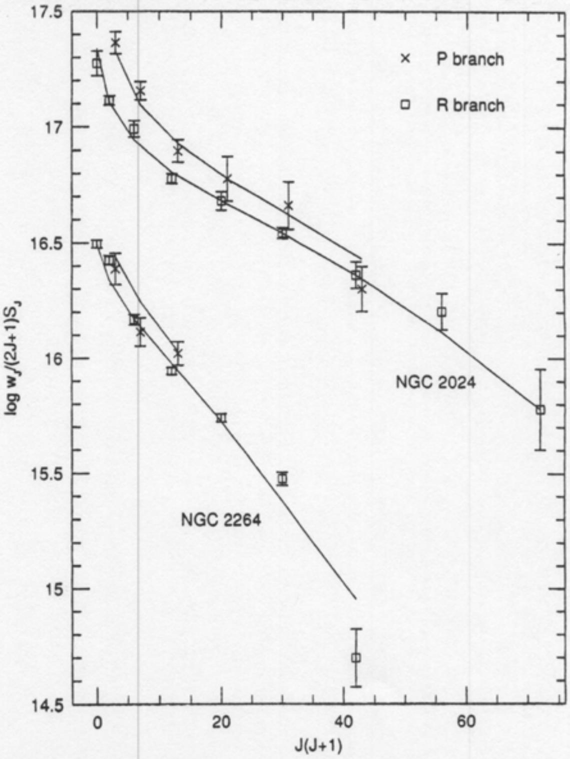

FIG. 2.—Values of log [N_J(thin) = $w_J/(2J + 1)S_J$] vs. $J(J + 1)$ for NGC 2024 IRS 2 and NGS 2264 (GL 989). Results from R-branch lines are shown as squares; results from P-branch lines are shown as crosses (and are offset to the right for clarity). Results for NGC 2264 are offset downward by 1.0. If unsaturated and at a single temperature, the points would fall along a straight line. The curves through the data are calculations assuming a Gaussian-line curve of growth. For NGC 2024, $b = 6.9 \times 10^{-3}$ cm^{-1}, $N = 9.1 \times 10^{18}$ cm^{-2}, and $T = 45$ K. For NGC 2264, $b = 2.0 \times 10^{-2}$ cm^{-1}, $N = 4.7 \times 10^{18}$ cm^{-2}, and $T = 30$ K.

saturation causing the curvature of the distribution. For NGC 2264, $b = 2.0(1.5\text{–}2.6) \times 10^{-2}$ cm^{-1}, $N_{CO} = 4.7(4.0\text{–}5.8) \times 10^{18}$ cm^{-2}, and $T = 30$ (28–32) K. Black et al. measured the CO linewidths toward NGC 2264 to be $b = 2.5 \times 10^{-2}$ cm^{-1}, in agreement with our curve-of-growth analysis. Toward both NGC 2024 and NGC 2264, our CO results are in good agreement with those of Black & Willner and Black et al.

Several systematic errors may affect our results. For H_2, our main concern is with possible filling-in of absorption with emission. Extended or broad-lined gas would be easily recognized, and was not seen. Probably the worst case would be if narrow $S(1)$ emission (like that toward Mon R2) just canceled the absorption. However, even in this case the effect on the $S(0)$ line would be small. In emission, $S(0)$ is typically 3 times weaker than $S(1)$, whereas in absorption at the temperatures we observe, it should be ~ 10 times stronger. Consequently, the ratio of emission to absorption for $S(0)$ would be $\sim 1/30$ even in the case of equal emission and absorption for $S(1)$. For CO, the main uncertainty is in the assumption of a Gaussian line. A line with stronger wings than a Gaussian would require a greater line-center optical depth to reproduce the observed P:R equivalent width ratios, and so a greater CO column density. Since our CO column densities are surprisingly large (see below), this seems unlikely. To fit our data on NGC 2024 with smaller optical depths would require a line with weaker wings than a Gaussian, but even in the extreme case of a rectangular line, our preferred value of N_{CO} would only drop to 7.5×10^{18} cm^{-2}.

4. DISCUSSION

At temperatures below 100 K, essentially all H_2 is in the $J = 0$ and $J = 1$ states. Consequently, the H_2 ortho:para ratio is given by the ratio of the populations of these two states. Our limit on the $J = 1 : J = 0$ ratio toward NGC 2024, <0.8 (2 σ), is significantly less than the expected ortho:para ratio of 3 when H_2 first forms, and is consistent with the value of 0.2 expected if it is thermalized at the temperature of the CO. Two processes are thought to be most important in modifying the ortho:para ratio in cold clouds: proton exchange reactions with H^+ and H_3^+, equilibrating ortho:para at the gas temperature, and interaction with magnetic impurities in grains, equilibrating ortho:para at the grain temperature (Burton, Hollenbach, & Tielens 1992). These processes are expected to equilibrate ortho:para in a time short compared to the lifetime of a molecular cloud. Our observations are consistent with this prediction.

For the purpose of determining the most probable value of N_{H_2} (H_2:CO), we assume that $J = 1 : J = 0$ is thermalized at the CO temperature; estimated grain temperatures are about equal to the gas temperatures (Thronson et al. 1984; Sargent et al. 1984). With this assumption, and using only our $S(0)$ measurement, we obtain $N_{H_2} = (3.5 \pm 1.4) \times 10^{22}$ cm^{-2} toward NGC 2024, and $<2.4 \times 10^{22}$ cm^{-2} toward NGC 2264 (2 σ uncertainties).

To determine the H_2:CO ratio, we fitted the H_2 and CO equivalent widths simultaneously. Toward NGC 2024 IRS 2, the best-fitting value of H_2: CO is 3900, with an allowed (2 σ) range of 1300–6800. The value of χ^2 for the fit is 10.6 for 12 degrees of freedom, indicating that the model fits the data well and the noise was estimated reasonably . Toward NGC 2264, the best-fitting value of H_2: CO is 1800, but N_{H_2} (and so H_2: CO) differs from 0 only at the 1 σ level. The upper limit on H_2: CO is 5200.

There are few other determinations of H_2: CO with which we can compare our measurements. Frerking, Langer, & Wilson (1982) compare the column densities of various CO isotopes with A_v, and obtain $N_{C^{18}O}/A_v = 1.7 \times 10^{14}$ cm^{-2} in cloud interiors ($A_v > 4$). This corresponds to $N_{CO}/A_v = 8.3 \times 10^{16}$ cm^{-2}, and H_2: CO = 12,000 if the low-A_v ratio of $N_H/A_v = 1.9 \times 10^{21}$ cm^{-2} (Bohlin, Savage, & Drake 1978) is assumed. Watson et al. (1985) made a direct measurement of H_2: CO = 8000 in the shocked gas in Orion, but it is unlikely that the abundances of H_2 and CO there are typical of molecular clouds. Wilson et al. (1986) observed warm gas in the same region, and obtained H_2: CO = 20,000. Most other papers on the subject (see van Dishoeck & Black 1987), discuss N_{H_2}/I_{CO}, not N_{H_2}/N_{CO}, and bypass the determination of I_{CO}/N_{CO}.

It is also of interest to compare N_{H_2} and N_{CO} to estimates of A_v toward our sources. The extinction to NGC 2264 (GL 989) is highly uncertain, with values in the literature ranging from $A_v = 5$ to $A_v > 35$. McGregor, Persson, & Cohen (1984) point out the complexity of the source, which in the near-infrared has diffuse extended emission and a pointlike condensation that is not coincident with the mid-infrared source.

Jiang, Perrier, & Lena (1984) measured $A_v = 21.5 \pm 5$ to NGC 2024 IRS 2, based on modeling to speckle interferometry and photometry. About half of the extinction may be due to circumstellar material (which may or may not contain H_2 and CO), as Maihara, Mizutani, & Suto (1990) used Brγ/Brα to derive $A_v \approx 11$ for the extended ionized gas surrounding the source. Assuming $A_v = 21.5$, we obtain $N_{H_2}/A_v \approx 1.7 \times 10^{21}$ cm^{-2} and $N_{CO}/A_v \approx 4.3 \times 10^{17}$ cm^{-2}, with uncertainties of factors $\sim$2. Our N_H/A_v is about 1.8 times that measured by Bohlin et al., whereas our N_{CO}/A_v is about 5 times that measured by Frerking et al. These results suggest that the gas-to-dust ratio toward NGC 2024 is nearly normal, and that it is the CO abundance that is surprising.

The N_{CO}/A_v ratios through the NGC 2024 and 2264 molecular clouds can also be estimated from longer wavelength observations. Toward NGC 2024 FIR 5, Graf et al. (1993) derived $N_{CO} = 2 \times 10^{19}$ cm^{-2} from CO emission, and Thronson et al. (1984) derived $A_v \approx 100$ from 60 μm dust emission, giving $N_{CO}/A_v \approx 2 \times 10^{17}$. A similar N_{CO}/A_v ratio, 2.2×10^{17}, through NGC 2264 is obtained from the results of Sargent et al. (1984) and Krügel et al. (1987). Both numbers are less than our determination, but probably not significantly so given the large uncertainty in the interpretation of the continuum observations.

Finally, our H_2: CO ratio may be compared to the solar H: C ratio of 2500 (Grevesse et al. 1991). Assuming all H to be in H_2, we conclude that about one-third of all carbon is in gas-phase CO. Although uncertain by a factor $\sim$2, this is a considerably larger fraction of carbon in CO than previously estimated. The column density of solid CO toward NGC 2024 is small (Tielens et al. 1991), but gas-phase C and C^+ together may be comparable to CO in abundance (Jaffe et al. 1994), suggesting that graphite and carbonate grains may contain only about one-third of all carbon.

We are grateful to D. Griep and W. Golisch for assistance with the observations, T. Greene for assistance in the use of CSHELL, and J. Achtermann for modifying Snoopy for reduction of CSHELL data. We also than the referee, S. P. Willner, for pointing out a significant error in the original *Letter*, and E. van Dishoeck and G. Mitchell for helpful discussions. This work was supported by grants from the NSF and USAF.

REFERENCES

Achtermann, J. M. 1992, in Astronomical Data Analysis and Software, ed. D. M. Worrall, C. Biemesderfer, & J. Barnes (ASP Conf. Ser., 25), 451
Black, J. H., van Dishoeck, E. F., Willner, S. P., & Woods, R. C. 1990, ApJ, 358, 459
Black, J. H., & Willner, S. P. 1984, ApJ, 279, 673
Bohlin, R. C., Savage, B. D., & Drake, J. F. 1978, ApJ, 224, 132
Burton, M. G., Hollenbach, D. J., & Tielens, A. G. G. M. 1992, ApJ, 399, 563
Frerking, M. A., Langer, W. D., & Wilson, R. W. 1982, ApJ, 262, 590
Goorvitch, D., & Chakerian, C. 1994, ApS, 91, 483
Graf, U. U., Eckart, A., Genzel, R., Harris, A. I., Poglitsch, A., Russell, A. P. G., & Stutzki, J. 1993, ApJ, 405, 249
Grevesse, N., Lambert, D. L., Sauval, A. J., van Dishoeck, E. F., Farmer, C. B., & Norton, R. H. 1991, A&A, 242, 488
Grossman, E. 1989, private communication
Jaffe, D. T., Zhou, S., Howe, J. E., Herrmann, F., Madden, S. C., Poglitsch, A., van der Werf, P. P., & Stacey, G. J. 1994, preprint
Jiang, D. R., Perrier, C., & Lena, P. 1984, A&A, 135, 249
Krügel, E., Güsten, R., Schulz, A., & Thum, C. 1987, A&A, 185, 283
Maihara, T., Mizutani, K., & Suto, H. 1990, ApJ, 354, 549
McGregor, P. J., Persson, S. E., & Cohen, J. G. 1984, ApJ, 286, 609
Sargent, A. I., Van Duinen, R. J., Nordh, H. L., Fridlund, C. V. M., Aalders, J. W. G., & Beitema, D. 1984, A&A, 135, 377
Thronson, H. A., Lada, C. J., Schwartz, P. R., Smith, H. A., Smith, J., Glaccum, W., Harper, D. A., & Loewenstein, R. F. 1984, ApJ, 280, 154
Tielens, A. G. G. M., Tokunaga, A. T., Geballe, T. R., & Baas, F. 1991, ApJ, 381, 181
Tokunaga, A. T., Toomey, D. W., Carr, J., Hall, D. N. B., & Epps, H. W. 1990, Proc. SPIE, 1235, 131
Turner, J., Kirby-Docken, K., & Dalgarno, A. 1977, ApJS, 35, 281
van Dishoeck, E. F., & Black, J. H. 1987, in Physical Processes in Interstellar Clouds, ed. G. E. Morfill & M. Scholer (Dordrecht: Reidel), 241
Watson, D. M., Genzel, R., Townes, C. H., & Storey, J. W. V. 1985, ApJ, 298, 316
Wilson, T. L., Serabyn, E., Henkel, C., & Walmsley, C. M. 1986, A&A, 158, L1

Shocks

upstream $v > C_s$

which is upstream?

example of wind-driven HII expansion

J shocks: jump; abrupt change $d \sim \frac{1}{n\sigma} \sim \frac{1000 AU}{n}$

C shocks: continuous: Alfvén wave precedes

in H_2 cloud: J if $v \gtrsim 40$ km/s

for typical $\vec{B}$, ionization

conservation equations: mass flux, momentum flux, energy flux

$$\rho_0 v_0 = \rho_1 v_1$$

$$\rho_0 v_0^2 + P_0 = \rho_1 v_1^2 + P_1$$

$$\frac{1}{2}\rho_0 v_0^3 + u_0 v_0 + P_0 v_0 = \frac{1}{2}\rho_1 v_1^3 + u_1 v_1 + P_1 v_1$$

u = internal E/V

$u + P$ = enthalpy/V

ideal gas: $P = nkT = \frac{\rho}{\mu} kT$

sound speed: $C_s^2 = \frac{dP}{d\rho}$

adiabatic: $P \propto \rho^\gamma$ $\quad \gamma = \frac{C_p}{C_v} = \frac{5}{3}$: monatomic

$\frac{7}{5}$: include diatomic rotation

$\frac{9}{7}$: include diatomic vib.

$C_s^2 = \gamma \frac{P}{\rho}$ or $P = \frac{\rho}{\gamma} C_s^2$

$$u = \frac{P}{\gamma - 1} = \frac{3}{2} nkT \quad \text{for } \gamma = \frac{5}{3}$$

Mach number: $\mathcal{M} = \frac{v_0}{C_{s,0}}$

J Shocks

Just downstream of a J shock can solve conservation equations (Tielens p. 400).

For $M \gg 1$ $\quad \frac{\rho_1}{\rho_0} = \frac{\gamma+1}{\gamma-1} = 4$ immediately after shock

$= 6 \quad \gamma = \frac{7}{5}$: H_2 w/ rotation

$= 8 \quad \gamma = \frac{9}{7}$: H_2 w/ vibration

note: t for rot. excitation $\sim 10^6$ s at $n \sim 10^4$
but molecules will radiate in similar time
especially if vibration is excited

for $\gamma = \frac{5}{3}$, P_0, u_0 small: $\quad P_1 = \frac{3}{4} \rho_0 v_0^2$

$v_1 = \frac{1}{4} v_0$

$kT_1 = \frac{3}{16} \mu v_0^2$

in ionized gas: $T_1 \approx 1.4 \times 10^5 \; v_{100}^2$

higher in neutral or molec. gas, but will dissociate quickly

For $T \gtrsim 10^5$ K $\quad t_{cool} \propto 1/n$ and increases w/ $T^{>1}$

$N_{cool} = n v t_{cool} \approx 2 \times 10^{17} \; v_{100}^{4.2}$ cm^{-2} (indep of n)

for $v_0 \approx 60-1000$ km/s

For slower shocks, the gas cools back toward T_0

Then $\rho_2 = M^2 \rho_0$ for $T_2 = T_0$ if unmagnetized

$v_2 = C^2/v_0 = v_0/M^2$

If magnetized, P_{mag} resists compression, and

$\frac{n_2}{n_0} \lesssim 80 \; v_{100} \; \underbrace{n_0^{1/2} / B_{\mu G}}_{\sim 1}$, $T_2 \lesssim 10^4 \; v_{100}$

Chemistry in J shocks

J shocks w/ $v_0 \gtrsim 25$ km s^{-1} dissociate molecules

H_2 reforms on dust in $N_{H_2} \approx 4 \times 10^{22}$ cm^{-2}

reformation heating keeps $T \sim 500$ K if $n \gtrsim 10^4$

warm chemistry produces CO, H_2O, OH, O_2, H_2S, SO, SO_2, SiO

J shocks are characterized by low ionization + high T compared to HII regions.

(or actually HII regions are characterized by ionization > T_{gas})

C Shocks

Alfvén waves in a plasma — magnetic restoring force

If $\nu \ll 1/t_{coll}$ betw. ions + neutrals, both ions + neutrals move. Then $v_A = \left(\frac{B^2}{4\pi\rho}\right)^{1/2}$

If $\nu \gg 1/t_{coll}$, only ions move and $v_{A,i} = X_c^{-1/2} v_A$

If $v_{Ai} > v_{shock} > C_s$: ions move ahead of shock, heating + acceleration gas gradually

Since gas radiates as it is heated, T never rises as high as in J shock. The result is a relatively thick layer at ≅ constant $T \sim 2000$, $\propto v_{shock}^{0.8}$

At this T, rot. + vib lines of H_2 + rot. lines of H_2O, CO are bright. (vib xitions of H_2O + CO are poorly excited.)